ELSEVIER

Journal of Hazardous Materials 72 (2000) 265–282

Journal of Hazardous Materials

www.elsevier.nl/locate/jhazmat

Air distribution during in situ air sparging: an overview of mathematical modeling

N.R. Thomson [a,*], R.L. Johnson [b,1]

[a] *Department of Civil Engineering, Faculty of Engineering, University of Waterloo, 200 University Avenue West, Waterloo ON, Canada N2L 3G1*

[b] *Department of Environmental Science and Engineering, Oregon Graduate Institute of Science and Technology, Beaverton, OR 97006, USA*

Abstract

The performance of in situ air sparging is controlled by the distribution of air pathways in the subsurface, which is in turn controlled by the structure of the medium to be sparged. The specific pathways that the air follows are determined, at the grain scale, by the distribution of air entry pressures of the pores. At the field scale, pore size distributions are usually correlated with heterogeneous structures (e.g. layers) within the medium, which control the macroscopic distribution of the air. The processes that produce an observed air distribution at a particular site are complicated, and are potentially well suited to modeling with multiphase flow models. Recent numerical modeling of heterogeneous media appears to successfully represent expected distributions of air; however, current models do not provide a tool to predict sparging performance. For this to be the case, the models need to represent the detailed structure of the medium at the site to be studied, as well as to capture the relevant aspects of the discrete air/water distribution (i.e., represent air channels at the centimeter or smaller scale). This will, in general, require a level of site data that is not available and numerical models that require many millions of computational elements. As a consequence, at least for the foreseeable future, numerical modeling of the air sparging process will continue to play a vital role as a conceptual tool with limited predictive capability at sites.

Keywords: Air sparging; Air distribution; Modeling; Two-phase flow; Simulation

* Corresponding author. Tel.: +1-519-888-4567, ext. 2111; fax: +1-519-888-6197; e-mail: nthomson@uwaterloo.ca

[1] Tel.: +1-503-690-1193; fax: +1-503-690-1273; e-mail: rjohnson@ese.ogi.edu

0304-3894/00/$ - see front matter
PII: S0304-3894(99)00143-0

1. Introduction

Primarily due to the limitations of pump-and-treat to remediate sources of groundwater contamination, various other technologies have been proposed. One technology that has gained widespread use at a number of sites is in situ air sparging (IAS) (e.g. Refs. [1,2]). IAS involves the injection of clean, pressurized air (or potentially other gases) into the saturated zone to treat contaminant sources trapped within water saturated and capillary zones, to remediate dissolved contaminant plumes, and to provide barriers to contaminant plume migration. IAS is widely used because it is often economical and easy to implement, and there are numerous reported successes. However, the sparging process is complicated and some of the underlying processes are not clearly understood.

IAS removes volatile organic compounds by volatilization, and adds oxygen to the ground water zone that aids in the aerobic biodegradation of some compounds. For either of these mechanisms to be effective, there must be favorable contact between the injected air and the contaminated groundwater as the removal of mass from source zones and plumes is limited by the amount of air contact. Therefore, a clear understanding of the migration pathways of the injected air is essential to aid in the design process, minimize cost, and maximize the success of the IAS system to achieve its objectives.

Mathematical models can be used to improve our understanding and ability to predict air migration patterns for different subsurface environments. The purpose of this paper is to provide an overview of mathematical modeling efforts in the context of our current understanding of the air distribution patterns taking place during IAS. This overview begins with a discussion of the conceptual model of air migration within the saturated ground water zone, and is followed by a description of the relevant aspects and assumptions inherent in multiphase flow theory. A summary of the important findings from previous mathematical model applications reported in the literature are presented and discussed. Finally, the results from some one- and two-dimensional numerical simulations are presented.

2. Conceptual model of air migration during IAS

The conceptual model of the injected air migration pathways within the saturated zone presented here builds on the conceptual models described by Johnson et al. [2] and Ahlfeld et al. [3], and recent laboratory and field observations. It will be assumed that the air is being injected into a short-screened injection point located within the saturated zone, and that the injection pressure is initially set at 5 to 40 kPa above hydrostatic pressure. In response to the application of pressurized air, the air/water interface within the injection point will be lowered over time until air begins to exit the injection point through the screen into the saturated medium. As air begins to move into the medium, the airflow will be small enough that the air delivery system will be able to maintain the injection pressure as the air expands out. Under these circumstances the air pressure is likely to be enough above hydrostatic that it will lead to substantial dewatering of the formation. This may occur for tens of centimeters to perhaps a meter away from the injection point.

After some short period of ''spherical'' growth of the air zone in the vicinity of the injection point, upward growth due to buoyancy will dominate; however, some lateral growth may continue as shown in Fig. 1(a). Once the air zone reaches the water table the pressure within the air zone will drop due to increased airflow to the vadose zone. This will cause the air zone to contract and probably represents the point at which water pressure within the medium stops increasing and begins to decrease. During the growth phase of the air zone, some pathways (channels) may be able to migrate laterally away from the central air zone and reach the water table. These channels may persist after the air zone reaches the water table, or they may collapse due to the reduced pressure at their source. In any event, these pathways are likely to be relatively isolated from one another and may have limited capacity to remove contaminants.

The bulk of the air/water contact for this homogeneous case will be in the central core area. Unfortunately, this area is likely to be on the order of a meter in radius. Furthermore, the high air content in the core may result in a substantial reduction in water permeability within this region. In a truly homogeneous medium, this entire process will most likely occur in a matter of minutes and the increased water pressure associated with air injection will be dissipated in less than 1 h.

However, virtually all naturally occurring media should be considered heterogeneous with regard to air sparging. It is useful to consider two conceptual cases for heterogeneous porous media. The first consists of a relatively permeable medium that contains very-low permeability strata (e.g. clay). The second is composed of zones of similar media whose permeabilities may vary over one to two orders of magnitude. In the first case, air will flow in the medium as described above until the upward-moving air

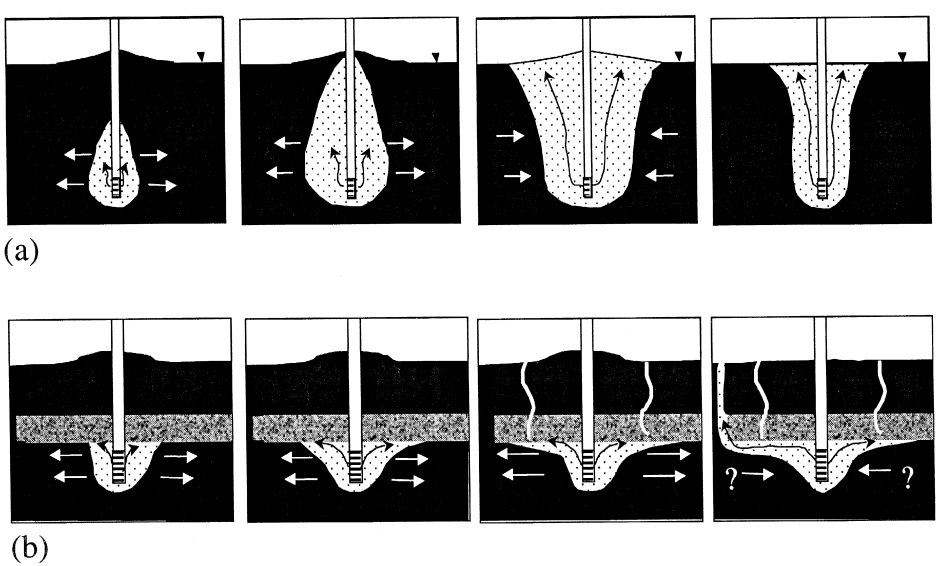

Fig. 1. Schematic representation of air distributions during IAS startup in (a) a homogeneous medium, and (b) in a layered heterogeneous medium.

contacts the bottom of a low permeability zone (Fig. 1b). For materials like clay, air entry pressures are generally larger than the differences between the hydrostatic and the injection pressures and, as a result, the air will not penetrate into the layer. Instead, the air will move laterally under the influence of the injection air pressure until the injection system can no longer maintain that pressure or until a vertical pathway is intersected. For continuous clay layers, this lateral movement may persist for many tens of meters and for a number of days. Ultimately, pathways such as monitoring wells or other discontinuities will allow sufficient air to migrate upwards that the lateral growth will stop. At that point, the increased water pressure associated with air injection will be dissipated. Air distribution in the second conceptual heterogeneous medium (spatially correlated zones where permeability varies over one to two orders of magnitude) is somewhat more complex. As the growth of the air zone around the well is initiated, and upward movement begins, the air will once again come in contact with lower permeability strata. In this case, depending upon the permeability contrast and the injection pressure, the air may or may not penetrate the layer. In general terms, it can be assumed that the ratio of the air entry pressures of two media are proportional to the ratios of the square roots of their permeabilities. Thus, if a medium sand with an air entry pressure of 0.3 m and a hydraulic conductivity of 10^{-4} m/s lies below a silty sand with hydraulic conductivity of 10^{-5} m/s, then the air entry pressure of the silty sand would be $\sim$1 m. One meter of water corresponds to approximately 0.1 atm or 1.5 psi, which is well within the range of excess pressures used during IAS startup. Thus, in this case, the air might penetrate through the layer. If the permeability contrast were two orders of magnitude, then the air entry pressure of the upper medium would be about 100 kPa (1 atm or 15 psi), which is well above the excess pressures used in sparging. In this case air would spread laterally until it found a vertical migration pathway.

For both of these heterogeneous cases, the air distribution will depend upon the lateral correlation scales of the layers (the characteristic length over which the correlation between point hydraulic conductivity values are statistically significant), the injection rate and the permeabilities of the medium, among other things, and will, in general, be very difficult to predict.

2.1. Field evidence of air distribution

Field data suggests that in ''homogeneous'' media the majority of the airflow is focused around the sparge point as inferred by Lesson et al. [4]. These authors observed sparge air breakthrough (from a uniform sand aquifer) at a saturated ground surface and found that the majority of airflow at the surface was within a 0.3 to 0.6 m radius around the injection point. In addition, there were a number of points at 1 to 5 m from the sparge location, which probably represent isolated channels of air moving up through the medium.

Lundegard and LaBrecque [5], using electrical resistance tomography (ERT), showed that within a relatively homogeneous sand medium (permeability of 2×10^{-12} m^2) the steady-state air distribution was fairly centralized around the sparge point and approximately parabolic in shape, with an estimated maximum air saturation between $\sim$20% and $\sim$40%. A similar air saturation distribution was reported by McKay and Acomb

[6], who used neutron probe data to estimate a maximum air saturation of ~30%. Both the rate of injection and the depth that the air is injected affect the lateral extent of sparge air, as observed by Lesson et al. [4] at the surface, and by McKay and Acomb [6] within the subsurface. However, the bulk of the airflow was always within a meter of the injection well for injection depths ranging up to 5.3 m below the water table.

Lundegard and LaBrecque [5] also used ERT measurements in a heterogeneous glacial till consisting of gravely sediments with interstratified silty sand. They observed lateral spreading of the injected air across their site with estimated air saturations below the strata greater than 50% and with little air reaching the water table in the vicinity of the sparge well. Tomlinson et al. [7] used both visual observations and a suite of geophysical tools to assess air distribution at a test site at CFB Borden. They observed that the air became trapped beneath a large number of small lenses within this relatively homogeneous medium, and that the air moved by a combination of lateral spreading and upward migration through those lenses. Johnson et al. [8] examined a layered medium to fine sand aquifer with interbedded clayey silts using SF_6 and dissolved oxygen as tracers and also found that the injected air spread laterally across the site until the injected air intersected a monitoring well. Field observations suggest that an increase in the air saturation below very low permeability layers leads to lateral spreading of the air and may limit the effectiveness of the IAS system by diverting air from the target area.

As is outlined above, it can be concluded that the structure of the medium plays a major role in controlling the air migration patterns, and the ultimate extent and nature of the sparge zone. Multiphase flow models have the potential to provide insight into the role of the various factors (e.g. aquifer structure, air injection rate, injection location, etc.) that make the prediction of air distribution extremely complicated.

3. Relevant aspects from multiphase flow theory

Assuming that the preceding conceptual model captures the essence of air migration and the ultimate steady-state air distribution within the saturated zone, then certain aspects from multiphase flow theory can be adopted in an attempt to mathematically model this process at the macroscopic scale. Perhaps the most important assumption from multiphase flow theory is that a porous medium is assumed to consist of two overlapping fluid continua (one air and the other water) where the fluid saturation is a function of space and time, and that these fluids occupy their own pathways according to a defined phase saturation. Hence, the permeability of each fluid within the porous medium is affected by the presence of the other phase giving rise to the relative permeability concept [9]. These assumptions allow Darcy's law to be extended to each fluid phase

$$q_{\beta i} = -\frac{k_{r\beta} k_{ij}}{\mu_\beta}\left(\frac{\partial P_\beta}{\partial x_j} + \rho_\beta g e_j\right) \quad i,j = 1,2,3 \tag{1}$$

where β represents either the water (w) or air (a) phase, $q_{\beta i}$ is Darcy's velocity for phase β in the ith coordinate direction, $k_{r\beta}$ is the relative permeability, k_{ij} is the

intrinsic permeability field, ρ_β is the phase density, μ_β is the absolute viscosity of the phase, P_β is the phase pressure, g is the gravitational acceleration, and e_j are the components of a unit vector in the positive z-coordinate direction $\langle 0,0,1\rangle$. Assuming a non-deformable medium, constant fluid viscosity, and applying the principle of mass conservation to each fluid phase yields

$$\frac{\partial(\phi\rho_\beta S_\beta)}{\partial t} = +\frac{\partial}{\partial x_i}\left[\frac{\rho_\beta k_{ij} k_{r\beta}}{\mu_\beta}\left(\frac{\partial P_\beta}{\partial x_j} + \rho_\beta g e_j\right)\right] + \Gamma_\beta \quad i,j = 1,2,3 \tag{2}$$

where ϕ is the porosity, S_β is the phase saturation and Γ_β is a fluid sink or source. Over the range of fluid pressures that are expected to occur during IAS the compressibility of the air phase must be considered, while the density of the water phase can be assumed to be constant. The density of the air phase may be assumed to be controlled by

$$\rho_a = \rho_a^o e^{c_a P_a} \cong \rho_a^o + c_a P_a \tag{3}$$

where ρ_a^o is the air density at $P_a = 0$ (zero gauge pressure), and c_a is the gas phase compressibility determined from the ideal gas law.

Associated with Eq. (2) is the capillary pressure constraint

$$P_{caw}(S_w) = P_a - P_w \tag{4}$$

and the saturation constraint

$$S_w + S_a = 1 \tag{5}$$

where $P_{caw}(S_w)$ is the macroscopic capillary pressure.

The capillary pressure is controlled by the radii of curvature of the air/water interface at the pore scale; however, Eq. (4) is applicable at the macroscopic scale and must be determined experimentally for a given porous medium, and is subject to considerable spatial variability. Many laboratory and field methods have been developed to measure the capillary pressure–saturation relationship. Tabular data are generated from these experiments and may be used in a model as a *look-up* table with some form of an interpolation/extrapolation algorithm; however, various closed-form parametric models have appeared in the literature that relate the macroscopic scale capillary pressure to the degree of water saturation. The following two expressions seem to have gained widespread acceptance

$$\begin{aligned} S_{we} &= \left[\frac{P_d}{P_{caw}}\right]^\lambda \quad P_{caw} > P_d \\ S_{we} &= 1.0 \quad P_{caw} \le P_d \end{aligned} \tag{6}$$

developed by Brooks and Corey [10], and

$$\begin{aligned} S_{we} &= \left[1 + (\alpha P_{caw})^n\right]^{-m} \quad P_{caw} > 0 \\ S_{we} &= 1.0 \qquad P_{caw} \le 0 \end{aligned} \tag{7}$$

developed by van Genuchten [11], with

$$S_{we} = \frac{S_w - S_{wr}}{1 - S_{wr}} \tag{8}$$

where S_{we} is the effective water saturation, S_{wr} is the residual water saturation, P_d is the displacement pressure, and α, m and n are empirical parameters that effect the slope or location of the inflection point of the capillary pressure–saturation curve. Fig. 2(a) presents typical capillary pressure–saturation curves for a sandy porous medium (3.3×10^{-2} cm/s) for the Brooks–Corey relationship (Eq. (6)), and for the van Genuchten relationship (Eq. (7)). For air sparging, it is the behavior of these relationships near complete saturation that will control the extent and nature of the air distribution. The Brooks–Corey relationship has a clearly defined displacement pressure, or critical capillary pressure, that must be exceeded before any air is allowed to penetrate a region, while the van Genuchten relationship will allow some air to penetrate the same region for any capillary pressure greater than zero.

Closed-form expressions for the relative permeability in Eq. (2) have been obtained by using either the capillary pressure–saturation relationship given by Eq. (6) or Eq. (7) in conjunction with the hydraulic conductivity model of Burdine [12], or Mualem [13]. The Brooks and Corey parametric model with the Burdine conductivity model yields

$$k_{rw} = (S_{we})^{\frac{2+3\lambda}{\lambda}} \tag{9}$$

$$k_{ra} = C(1 - S_{we})^2 \left(1 - S_{we}^{\frac{2+\lambda}{\lambda}}\right) \tag{10}$$

while the van Genuchten model with $m = 1 - 1/n$ and the Mualem model produces

$$k_{rw} = S_{we}^{1/2}\left[1 - \left(1 - S_{we}^{1/m}\right)^m\right]^2 \tag{11}$$

$$k_{ra} = C(1 - S_{we})^{1/2}\left(1 - S_{we}^{1/m}\right)^{2m} \tag{12}$$

where C is the Klinkenberg factor that accounts for the air slippage in the air/water flow system [9].

A variety of solution methods exist to solve Eq. (2), with Eqs. (3)–(5), and either Eqs. (6), (9) and (10), or Eqs. (7), (11) and (12) in conjunction with a physically based set of initial and boundary conditions. The most common methods are the finite difference, finite element, or the finite volume methods, which essentially replace the governing equation (Eq. (2)) with a system of algebraic equations.

Unfortunately, the capillary pressure–saturation relationship is subject to hysteresis due to variations in the air/water contact angle that occurs during drainage or imbibition (wetting) [9]. This makes either capillary pressure–saturation relationship given by Eq. (6) or Eq. (7) non-unique for a specified value of water saturation. As air is initially

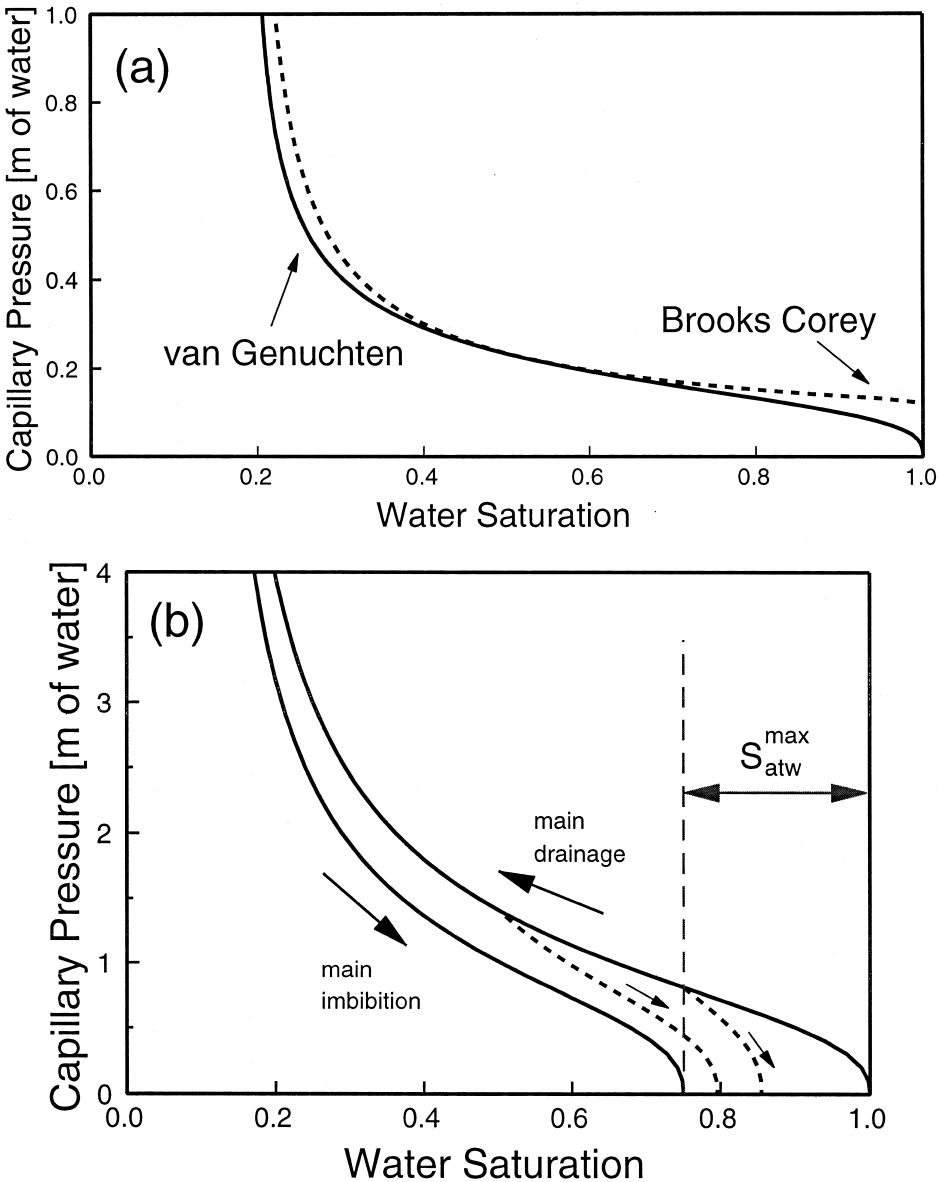

Fig. 2. (a) Typical capillary pressure–saturation curves fit to the same data for the Brooks–Corey relationship ($S_{wr} = 0.20$, $P_d = 1250$ Pa, $\lambda = 1.6$) and for the van Genuchten relationship ($S_{wr} = 0.20$, $n = 3.16$, $m = 1 - 1/n$, $\alpha = 0.0006/\text{Pa}$). (b) Capillary pressure–saturation curve showing impact of air entrapment.

injected into a water-saturated medium, the water at a particular location, say point P, within the sparge zone is slowly displaced by the injected air, and the capillary pressure–saturation relationship will follow the main drainage curve as shown in Fig.

2(b). If the capillary pressure at P was increased to a high enough level, than the water saturation would be reduced to S_{wr}. Assuming that this is the case at P, and then the air compressor was shut-off, the air pressure would decrease along with the capillary pressure, and capillary pressure–saturation relationship would follow along the main imbibition curve. When the capillary pressure at point P reached a value of zero, a certain amount of non-mobile or entrapped air would remain due to by-pass and snap-off mechanisms [14], as indicated by S_{atw}^{max} in Fig. 2(b). The saturation of this entrapped air has been reported to be > 0.1 for typical sandy soils, and has significant implications for dissolved oxygen transport and biodegradation [15]. Since it is possible to initiate the imbibition process at any point along the drainage curve, or the drainage process at any point along the imbibition curve, there exists a family of scanning curves that connect the main drainage and imbibition curves. To account for this level of complexity, a full hysteretic capillary pressure–saturation model similar to that presented by Parker and Lenhard [16] would be required. A less complex hysteretic model can be developed by ignoring the hysteresis in the capillary pressure–saturation relationships, but considering the impact of air entrapment. This hysteretic air entrapment model can be developed by considering the maximum possible air entrapment saturation in conjunction with the water saturation at the drainage to imbibition reversal point, S_w^r. Instead of allowing the capillary pressure–saturation relationship to be a function of the effective water saturation S_{we}, it is defined in terms of

$$S_{we}^{app} = \frac{(S_w - S_{wr})}{(1 - S_{wr})} + \frac{S_{atw}}{(1 - S_{wr})} = S_{we} + S_{atwe} \tag{13}$$

where S_{we}^{app} is the apparent water saturation, and S_{atw} and S_{atwe} are the actual and effective saturation of air trapped in water, respectively. The effective saturation of air trapped in water is linearly related to the maximum possible entrapped air saturation based on the water saturation reversal point given by

$$S_{atwe} = S_{atwe}^{max*}\left(\frac{S_{we}^{app} - S_{we}^{r}}{1 - S_{we}^{r}}\right) \tag{14}$$

and the maximum possible entrapped air saturation S_{atwe}^{max*} is from the following empirical relationship observed by Land [17]

$$S_{atwe}^{*} = \left(\frac{1 - S_{we}^{r}}{1 + R_{aw}(1 - S_{we}^{r})}\right) \quad R_{aw} = \frac{(1 - S_{wr})}{S_{atw}^{max}} - 1 \tag{15}$$

with

$$S_{atwe}^{*} = \frac{S_{atw} - S_{wr}}{1 - S_{wr}} \quad S_{we}^{r} = \frac{S_w^r - S_{wr}}{1 - S_{wr}} \tag{16}$$

where S_{we}^{r} is the effective water saturation at the reversal point. The relative permeability of the air and water phase is altered accordingly by the presence of the entrapped air.

4. Overview of previous model applications

Several attempts to model the air sparging process using concepts from multiphase flow theory have appeared in the published literature. Perhaps the first use of a multiphase flow model to simulate air sparging was by Lundegard and Andersen [18]. They used a modified version of the finite difference model TETRAD [19], which was developed for petroleum reservoirs. The focus of their investigation was on temporal and spatial variations in air distribution. A closed-form power law relationship was used to define the relative permeability of each phase, and the role of capillary pressure was ignored. All of their reported simulations were undertaken on an axisymmetric domain with a radius of ~ 120 m and a depth of ~ 30 m. The spacing of the rows were uniform at ~ 0.6 m, except near the initial water table location where the spacing was reduced to ~ 0.15 m, while the column spacing was increased by a factor of 1.5 in the radial direction, with an initial block radius near the sparge well of ~ 0.1 m. Their simulation results were able to capture the transient nature of the air distribution starting from the initial expansion phase, through the collapse phase as the injected air breaks through into the vadose zone, and finally to a steady-state configuration. A sensitivity analysis showed that the region influenced by the injected air will (a) not change with the injection depth, (b) will increase with an increase in air injection rate, and (c) will increase with an increase in the anisotropy ratio (k_{xx}/k_{yy}). A number of additional simulations with low permeability layers inserted into the axisymmetric domain above the injection point indicated the role of such features on the collection, or trapping, of air beneath these features. This process would have been accentuated if capillary pressure had been considered.

McCray and Falta [20] used a multiphase flow model (T2VOC) based on the integrated finite difference method to simulate the two-dimensional physical model experiments reported by Ji et al. [21]. The van Genuchten capillary pressure–saturation relationship given by Eq. (7) was used along with a closed-form power law relative permeability relationship for both the water and air phase. A rectangular 0.7×0.9 m spatial domain was discretized into ~ 0.03 m^2 grid blocks. Since the actual air phase saturations from the physical model experiments are not known, a quantitative comparison to the steady-state results was undertaken. Overall, the simulation model replicated the steady-state air flow patterns for both simulated experiments. However, a continuous range of air saturations was produced throughout the sparge zone by the model, and not the series of discrete continuous channels as were observed in the physical model. This is a direct result of the assumption that the medium is homogeneous at all scales. Using the same model in an axisymmetric configuration, Hein et al. [22] were able to replicate the measured gas phase flux from a three-dimensional physical model with a radius of

Fig. 3. (a) Comparison of the one-dimensional air sparging analytical solution (solid lines) to the numerical model simulation results (dashed lines) for four different air injection rates (soil permeability of 1×10^{-12} m^2, air viscosity of 1×10^{-5} Pa s, and water density of 1000 kg/m^3). (b) Temporal evolution of the air saturation distribution for an injection rate of 4.72×10^{-4} m^3/s. (c) Impact of air entrapment on the air distribution during collapse of the sparge zone after the air injection was terminated.

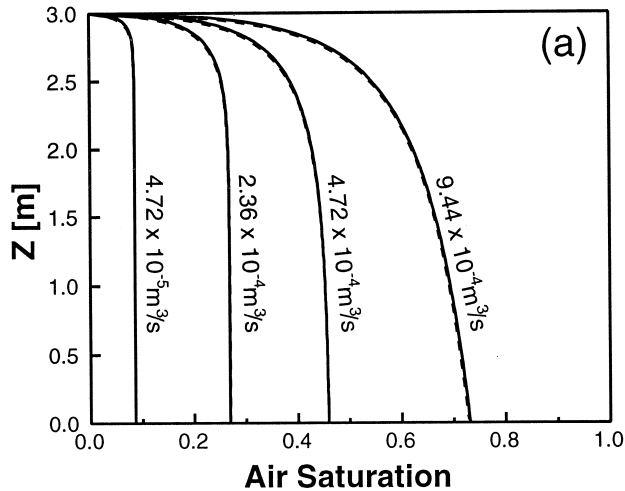
(a)
Z [m]
Air Saturation
4.72 x 10-5m3/s
2.36 x 10-4m3/s
4.72 x 10-4m3/s
9.44 x 10-4m3/s

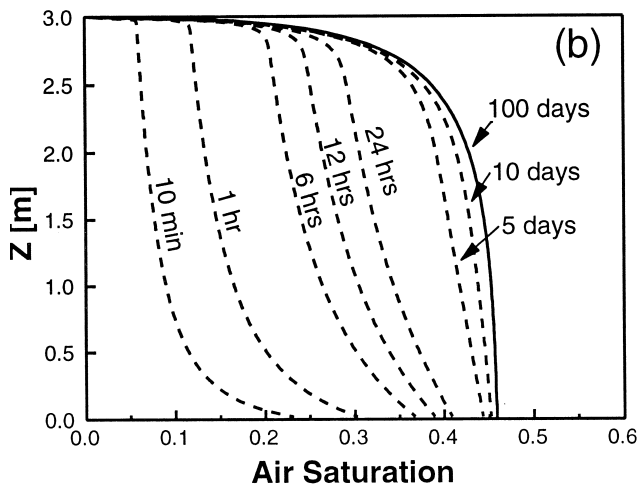
(b)
Z [m]
Air Saturation
10 min
1 hr
6 hrs
12 hrs
24 hrs
100 days
10 days
5 days

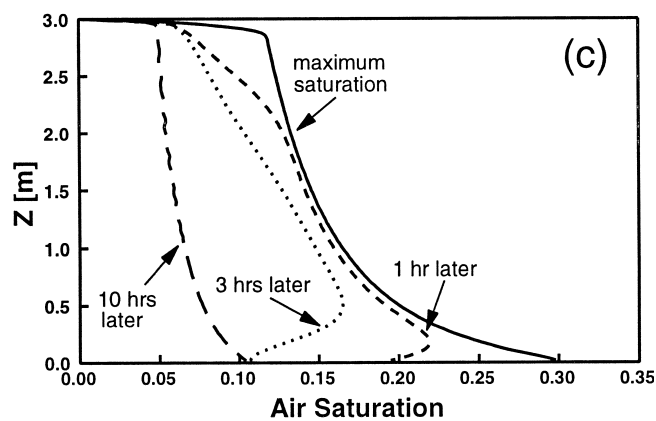
(c)
Z [m]
Air Saturation
maximum saturation
10 hrs later
3 hrs later
1 hr later

$\sim$0.6 m, and a depth of $\sim$0.65 m. This simulation domain was discretized into blocks ranging from 0.02 to 0.04 m in the radial dimension, and 0.04 m in the vertical dimension. Again the van Genuchten capillary pressure–saturation relationship given by Eq. (7) was employed along with a closed-form power law relative permeability relationship. The gas phase flux, which was measured by a flow-measuring device within a radius of 0.09 m, was compared to interpolated model results. In the near well region the model under predicted the flux by up to 40%. As suggested by the authors this discrepancy may be a product of an incorrect capillary pressure–saturation representation; however, it is more likely that this difference is due to the scale of the channels which are associated with the heterogeneous nature of the material within the physical model, which was not considered in the numerical simulations.

Van Dijke and van der Zee [23] used an axisymmetric finite element based multiphase model to investigate air flow regimes that developed in a layered soil. The van Genuchten capillary pressure–saturation relationship was used along with the relative permeability function given by Eqs. (11) and (12). They identified the following three distinct air flow regions that occur at steady-state: (1) the region from the well screen to below a lower permeability layer where buoyancy (gravity) forces dominate the primarily vertical flow, (2) the region just below the lower permeability layer where the air is spreading laterally and the capillary forces are of the same magnitude as the gravity forces, and (3) the region above this lower permeability layer and below the water table, where once again buoyancy forces dominate the flow. These authors go on to develop an analytical approximation that may be useful to estimate the radial spreading of the injected air that occurs below these horizontal lower permeability features.

In their study of the mechanisms which control the removal of mass from a heterogeneous medium, Unger et al. [24] used horizontal air sparging wells to deliver the air phase. The model used in their investigation, CompFlow, is a control volume based three-dimensional, three-phase compositional model. Stone's second method [25] was used to describe the relative permeability functions, while tabular data was used to describe the capillary pressure–saturation relationship. A $10 \times 10 \times 5$ m simulation domain was considered, and was discretized into finite volumes of the dimension $0.5 \times 0.5 \times 0.1$ m. A heterogeneous permeability field with a specified mean, variance and spatial correlation structure was generated, thus allowing each control volume to be assigned a unique value. The capillary pressure–saturation curves for each control volume were scaled using a modified form of the Leverett function [26]. The simulation results show that the injected air was trapped under the lower permeability layers similar to the physical model observations by Ji et al. [21].

In general, the application of multiphase flow theory to simulate the air distribution that occurs during IAS has been encouraging. Specifically, the simulation results capture the general air flow patterns that have been observed in laboratory and field IAS applications, which are consistent with the conceptual model discussed in Section 2. However, they do not produce channels of the same dimensions as observed in most field and laboratory experiments. This is due in part to the numerical resolution (e.g. grid size) used in the models. A consequence of the inability of the models to produce the channel structure is that mass transfer estimates from these models will not be realistic. In addition, the level of input data needed to accurately represent a field site

Table 1
Soil and fluid properties for Example 2

Property	Value
Permeability	1×10^{-12} m^2
Porosity	0.35
n	2.0
α	0.0002/Pa
S_{wr}	0.1
Water density	1000 kg/m^3
Water viscosity	1.0×10^{-3} Pa s
Air density	1.2 kg/m^3
Air viscosity	1.0×10^{-5} Pa s

(i.e. permeabilities, capillary-pressure saturation curves) far exceeds the data available at any site and, as a result, predictive modeling of actual sites is not currently possible.

5. Examples

Following the work by Forsyth [27], a control volume (CV)-based three-dimensional three-phase flow and transport model was developed. For air sparging applications, this model solves the two-phase flow equation given by Eq. (2) in a Cartesian coordinate system for a compressible air phase. Either the van Genuchten or Brooks–Corey capillary pressure–saturation relationship may be used along with the associated relative permeability relationships given by Eqs. (9)–(12). A hysteretic air entrapment model for the van Genuchten capillary pressure–saturation relationship has also been incorporated in the model. Several one- and two-dimensional examples using this approach are discussed below.

5.1. Example 1: one-dimensional problem

To test the ''predictive'' capabilities of this model, and to demonstrate the role that air entrapment may be expected to play during air sparging, the results from the

Table 2
Statistical properties of the random permeability fields used in Example 2
The geometric mean permeability for each generated field was 1×10^{-12} m^2.

Field	Variance	Correlation-x [m]	Correlation-y [m]
1	0.1	0.1	0.1
2	0.5	0.1	0.1
3	0.1	4.0	0.2
4	0.5	4.0	0.2

developed numerical model were compared to the results from a one-dimensional analytical solution developed by McWhorter [28]. The analytical solution assumes that a steady-state condition has been reached for each fluid phase, a uniform injection of air

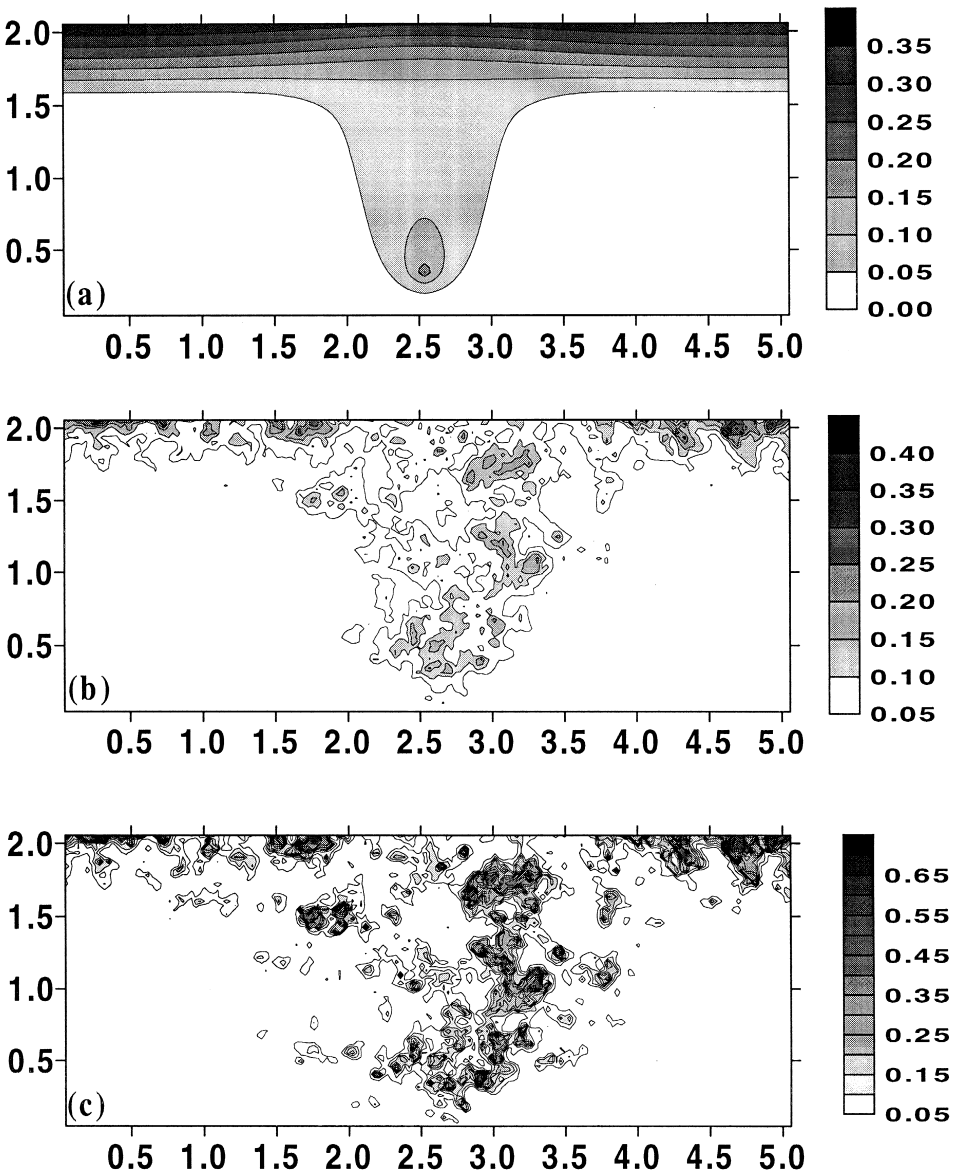

Fig. 4. Steady-state air distribution for each of the permeability fields investigated, (a) homogeneous permeability, and (b) to (e) correspond to Fields 1 to 4, respectively. Note that the air saturation contours intervals are different.

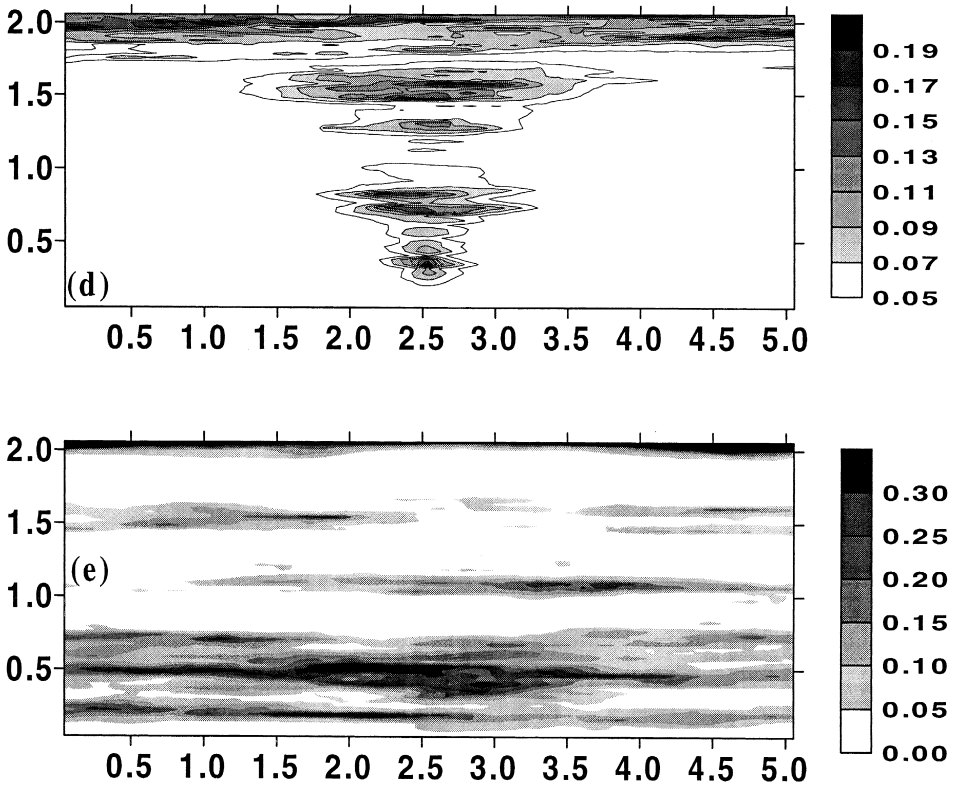

Fig. 4. (continued)

occurs at $Z = 0$, and air exits the saturated zone at $Z = L$ with a capillary pressure equal to the displacement pressure. The solution to this problem is given by

$$Z = L - \int_{P_d}^{P_{caw}(Z)} \left[\frac{q_a \mu_a}{k k_{ra}(P_{caw})} - \rho_w g \right]^{-1} \mathrm{d}P_{caw} \tag{17}$$

where q_a is the air injection flow rate, k is the permeability, k_{ra} is the relative permeability relationship which is expressed as a function of the capillary pressure P_{caw}. To use Eq. (17), the air saturation at a specified point Z in the one-dimensional spatial domain $[0, L]$ is determined by choosing the capillary pressure and hence the air saturation in an iterative fashion.

Fig. 3(a) presents a comparison of the analytical solution given by Eq. (17) to the model results using the van Genuchten capillary pressure–saturation relationship with $n = 2$, α of 0.002/Pa, and a residual water saturation of zero for air injection rates ranging from 4.72×10^{-5} to 9.44×10^{-4} m^3/s. In each of these cases investigated, the developed model compares very well with the analytical solution. Fig. 3(b) shows the temporal evolution of the air saturation from early time to the steady-state distribution for an air injection rate of 4.72×10^{-4} m^3/s. Notice that for this problem it takes

almost 100 days before the air distribution predicted by numerical model reaches steady-state. This is an attribute of the one-dimensional nature of this problem.

To demonstrate the impact of air entrapment on the air distribution, the numerical model was run for the same one-dimensional domain with an air injection rate of 4.72×10^{-4} m^3/s for 1 h, and then the air injection was terminated. Assuming a maximum entrapped air in water saturation (S_{atw}^{max}) of 0.25, the air distribution as the sparge zone is collapsing is presented in Fig. 3(c) for three times after the air injection was terminated. The air saturation profile 10 h after the airflow was stopped represents an essentially non-mobile situation. Notice that trapped air is present throughout this one-dimensional profile, and that the saturation is greater near the bottom of the profile where a larger maximum air saturation was attained.

5.2. Example 2: two-dimensional heterogeneous simulations

As discussed above, development of the air distribution away from the injection well screen is controlled by spatial variations in permeability, and therefore capillary pressure. To illustrate how this variation affects the resulting air distribution, four two-dimensional random permeability fields were synthesized and the resulting steady-state air distribution were investigated.

A 5.1×2.1 m spatial domain was selected for this investigation and was discretized into 0.025×0.025 m control volumes. The top boundary was assigned an air phase pressure of zero representative of atmospheric conditions, and the bottom boundary was assigned a water phase pressure equivalent to 1.4 m of water. Air was injected at a constant rate of 4.74×10^{-5} m^3/s at a single point located in the center of the domain ~ 0.35 m from the bottom. The van Genuchten capillary pressure–saturation relationship and the Mualem conductivity model were employed for all the simulations. Table 1 contains a list of the relevant soil and fluid properties used. Each of the random permeability fields was generated using the algorithm developed by Robin [29] based on Fast Fourier Transform spectral techniques. This is the same algorithm used by Unger et al. [24]. The geometric mean, variance, and spatial correlation length for each of the four permeability fields are presented in Table 2. The same random seed value was used to generate each of the permeability fields in order that any changes in the simulated air distribution could be attributed to changes to the underlying variance and spatial correlation structure. Fields 1 and 2 were assigned the same isotropic spatial correlation structure, but a difference variance, while Fields 3 and 4 were assigned a spatial correlation structure representative of the Borden aquifer, but a different variance. The empirical parameter α in the van Genuchten capillary pressure–saturation relationship was scaled following the theory of Leverett [26] for each control volume.

The air saturation distributions simulated for each of the permeability fields along with the homogeneous case are shown in Fig. 4. As expected a parabolic shaped air distribution resulted from the homogeneous permeability field with a maximum air saturation near 0.25 at the air injection location. The simulated air distribution using Fields 1 and 2 show a similar asymmetric air distribution pattern with the bulk of the air flow following a lower capillary pressure pathway located to the right-hand side of the air injection point. Along this pathway, the maximum air saturation was ~ 0.25 for

Field 1, while for Field 2, it was ~ 0.4. This is a direct result of the higher variance used to generate Field 2 than Field 1, which produced a larger range of permeabilities and hence capillary pressures. Unlike the simulated air distributions for Fields 1 or 2, the air distribution for Fields 3 and 4 coincide with the spatial correlation structure. Field 4, with its higher variance, produces flat low permeability/high capillary pressure layers like those found within layered sand aquifers. These features tend to trap the injected air underneath them, and cause the air to migrate laterally as shown in Fig. 4(e).

Although the numerical resolution is inadequate to produce discrete air channels, the steady-state air distributions produced from these few simulations provide an indication of the role that geologic heterogeneities play in actual IAS applications.

6. Conclusion

The distribution of air that results from air sparging within a saturated aquifer is controlled by microscopic and macroscopic processes. At the pore-scale it is the variation in air entry pressures that govern the migration of the injected air; while at the macroscale it is the presence of lower permeability zones that will alter the bulk air migration patterns. The actual mechanisms that control the air channel formation at a particular site will represent a coupling of the processes at these two scales, and thus will dictate the subsequent mass removal effectiveness of the sparging system.

Multiphase flow models have the potential to provide insight into the various factors controlling the air distribution. To date, these models have generally done a good job at capturing the bulk air distribution in both homogeneous and heterogeneous media; however, these models have not done such a good job at representing the details of the air distribution (e.g. channels). As a consequence, these models will not be effective as predictive tools for air sparging performance.

In order to be predictive of field performance, model discretization will need to be at less than the 10 cm scale. This scale is well below the level of detail that a medium can generally be characterized at sites. Assuming that this level of characterization is possible for a typical sparge target volume of the size $10 \times 10 \times 5$ m; than the required number of computational nodes, grid blocks, or control volumes would be in excess of a few million. This argument assumes that a brute force approach to the problem is adopted, and begs for the development of a new mathematical approach to air sparging.

References

[1] C.P. Ardito, J.F. Billings, Proceedings of the Petroleum Hydrocarbons and Organic Chemicals in Groundwater Conference, Detection and Restoration, Natl. Water Well Assoc., Dublin, OH, 1990, pp. 281–296.

[2] R.L. Johnson, P.C. Johnson, D.B. McWhorter, R.E. Hinchee, I. Goodman, Ground Water Monit. Rem. 13 (4) (1993) 127–135.

[3] D.P. Ahlfeld, A. Dahmani, W. Ji, Ground Water Monit. Rem. 14 (3) (1994) 132–139.

[4] A. Lesson, R.E. Hinchee, G.L. Headington, C.M. Vogel, Proceeding from the Third International In Situ and On-site Bioreclamation Symposium, 1995, pp. 215–222.

[5] P.D. Lundegard, D. LaBrecque, Remediation, Summer, 1998, pp. 59–71.
[6] D.J. McKay, L.J. Acomb, Ground Water Monit. Rem. 16 (4) (1996) 86–94.
[7] D.W. Tomlinson, N.R. Thomson, R.L. Johnson, J.D. Redman (1999) (in preparation).
[8] P.C. Johnson, R.L. Johnson, C. Neaville, E.E. Hansen, S.M. Stearns, I.J. Dortch, Ground Water 35 (5) (1997) 765–774.
[9] J. Bear, Dynamics of Porous Media, Dover Publications, New York, 1972, 764 pp.
[10] R.H. Brooks, A.T. Corey, Hydrology Paper No. 3, Colorado State Univ., Fort Collins, 1964, 27 pp.
[11] M.Th. Van Genuchten, Soil Sci. Soc. Am. J. 44 (1980) 892–898.
[12] N.T. Burdine, Petrol. Trans., Am. Inst. Min. Eng. 198 (1953) 71–77.
[13] Y. Mualem, Water. Resour. Res. 12 (1976) 513–522.
[14] F.A.L. Dullien, Porous Media, Academic Press, San Diego, CA, 1992, p. 574.
[15] V.A. Fry, J.D. Istok, K.T. O'Reilly, Ground Water 34 (2) (1996) 200–210.
[16] J.C. Parker, R.J. Lenhard, Water Resour. Res. 23 (12) (1987) 2187–2196.
[17] C.S. Land, Trans. Am. Inst. Min., Metall. Pet. Eng. 243 (1968) 149–156.
[18] P.D. Lundegard, G. Andersen, Ground Water 34 (3) (1996) 451–460.
[19] P.D.W. Vinsome, G.M. Shook, J. Pet. Sci. Eng. 9 (1993) 29–38.
[20] J.E. McCray, R.W. Falta, Ground Water 35 (1) (1997) 99–110.
[21] W. Ji, A. Dahmani, D.P. Ahlfeld, J.D. Lin, E. Hill III, Ground Water Monit. Rem. 13 (4) (1993) 115–126.
[22] G.L. Hein, J.S. Gierke, N.J. Hutzler, R.W. Falta, Ground Water Monit. Rem. (1997) 222–230.
[23] M.I.J. van Dijke, S.E.A.T.M. van der Zee, Water Resour. Res. 34 (3) (1998) 341–353.
[24] A.J.A. Unger, E.A. Sudicky, P.A. Forsyth, Water Resour. Res. 31 (8) (1995) 1913–1925.
[25] K. Aziz, A. Settari, Petroleum Reservoir Simulation, Applied Science, Essex, UK, 1979.
[26] M.C. Leverett, Trans. Am. Inst. Min., Metall. Pet. Eng. 142 (1941) 152–169.
[27] P.A. Forsyth, Adv. Water Resour. 11 (2) (1988) 74–83.
[28] D. McWhorther, personal communication, 1995.
[29] M.J.l. Robin, PhD Thesis, Univ. of Waterloo, 1991.